Published in final edited form as:

Appl Phys Lett. 2016 ; 109: .

Phonon Anharmonicity in Bulk T_d-$MoTe_2$

Jaydeep Joshi[1], **Iris Stone**[1], **Ryan Beams**[2], **Sergiy Krylyuk**[2], **Irina Kalish**[2], **Albert Davydov**[2], **Patrick Vora**[1,a]

[1]Department of Physics and Astronomy, George Mason University, Fairfax, VA 22030, USA

[2]Material Measurement Laboratory, National Institute of Standards and Technology, Gaithersburg, MD 20899, USA

Abstract

We examine anharmonic contributions to the optical phonon modes in bulk T_d-$MoTe_2$ through temperature-dependent Raman spectroscopy. At temperatures ranging from 100 K to 200 K, we find that all modes redshift linearly with temperature in agreement with the Grüneisen model. However, below 100 K we observe nonlinear temperature dependent frequency shifts in some modes. We demonstrate that this anharmonic behavior is consistent with the decay of an optical phonon into multiple acoustic phonons. Furthermore, the highest frequency Raman modes show large changes in intensity and linewidth near $T \approx 250$ K that correlate well with the $T_d \rightarrow 1T'$ structural phase transition. These results suggest that phonon-phonon interactions can dominate anharmonic contributions at low temperatures in bulk T_d-$MoTe_2$, an experimental regime that is currently receiving attention in efforts to understand Weyl semimetals.

I. INTRODUCTION

Transition metal dichalcogenides (TMDs) exhibit a wide range of layer-dependent phenomena depending on the choice of the transition metal and chalcogen atoms. Beginning with the discovery of photoluminescence from monolayer MoS_2,[1,2] most studies of TMDs have focused on the semiconducting $2H$ crystal phase in MoS_2, $MoSe_2$, WS_2, WSe_2, and $MoTe_2$.[3–8]. However, TMDs can exist in multiple structural phases that exhibit unique electronic properties, including the $2H$ (α, hexagonal, space group $P6_3/mmc$), $1T'$ (β, monoclinic, space group $P2_1/m$), and T_d (γ, orthorhombic, space group $Pnm2_1$) crystal phases.[9–11] The $2H$ structure is similar to the honeycomb lattice of graphene, but has broken sublattice symmetry and therefore a large bandgap ranging from 1–2 eV. For most TMDs, $2H$ is the dominant structural phase due to large ligand-field stabilization energies.[11] However, for $MoTe_2$ the ground-state energy difference between the $2H$ and the $1T'$ phases is minimal,[11,12] allowing both to be realized experimentally under ambient conditions. $1T'$-$MoTe_2$ has a distorted octahedral (monoclinic) structure and has been synthesized by a modified growth method[13–16] as well as a low-temperature solution phase synthesis procedure,[17] and has recently been found to be a low-bandgap semiconductor when in few-

[a] pvora@gmu.edu.

SUPPORTING INFORMATION

See supporting information for the analysis of Peak 1 and a discussion of the Raman tensors of $1T'$ and T_d $MoTe_2$.

layer form.[13] In addition, laser heating can drive $MoTe_2$ out of the $2H$ phase into a metallic phase with a Raman spectrum distinct from $1T'$-$MoTe_2$,[18] a discovery that potentially enables $MoTe_2$ metal-semiconductor homojunctions as well as phase change memories.[19]

$1T'$-$MoTe_2$ transitions into T_d-$MoTe_2$, an orthorhombic phase with broken inversion symmetry, when cooled below $T \approx 250$ K. This $1T' \rightarrow T_d$ transition in $MoTe_2$ has been observed in temperature-dependent electrical measurements as hysteresis after a warming/cooling cycle,[15,20–22] low-temperature Raman spectra through the activation of an inversion-symmetry forbidden shear mode,[22,23] X-ray diffraction (XRD) measurements,[24,25] and electron diffraction measurements.[26] The lattice constants in T_d-$MoTe_2$ and $1T'$-$MoTe_2$ are only slightly different[10,15,25] but nevertheless lead to striking modifications of the electronic structure, the most notable of which is the prediction of a type II Weyl semimetal phase.[27] This exciting electronic state has also been predicted in WTe_2[28] and the alloy $Mo_xW_{1-x}Te_2$,[29] and recent experimental results have confirmed the presence of the Weyl semimetal state in all three systems.[30–38]

The clear importance of T_d-$MoTe_2$ demands a systematic investigation of its properties and how they evolve under external stimuli. For example, high pressure has been shown to increase the superconducting transition temperature in T_d-$MoTe_2$ substantially.[15] Thus far there has been little work on understanding how the vibrational properties evolve with temperature[22,23] and the role of electron-phonon or phonon-phonon interactions in $1T'$ or T_d-$MoTe_2$, both of which play important roles in the electronic properties of materials. Understanding the origin of anharmonic effects in $MoTe_2$ is therefore important for futur explorations of low-temperature phenomena.

Here, we use temperature-dependent Raman spectroscopy to characterize anharmonic contributions to four prominent optical phonon modes in bulk T_d-$MoTe_2$. Our measurements extend down to 5 K, allowing us to observe departures from the commonly-observed Grüneisen behavior. We find that two phonon modes exhibit modest changes in frequency with temperature, while the remaining two modes exhibit large, nonlinear changes in linewidth, frequency, and intensity. All four modes exhibit a change in frequency and slope around $T \approx 250$ K, which correlates well with the $T_d \rightarrow 1T'$ structural phase transition. These observations are consistent with a regime where anharmonic contributions arising from optical phonon decay into multiple acoustic phonons are substantial.[39] Our results are the first studies of phonon anharmonicity in T_d-$MoTe_2$ and provide crucial information for understanding the low-temperature electronic and vibrational properties of this highly-relevant material.

II. EXPERIMENTAL METHODS

$MoTe_2$ single crystals were produced by the chemical vapor transport (CVT) method with iodine as the transport agent. First, $MoTe_2$ powder was synthesized by annealing a stoichiometric mixture of molybdenum (99.999%) and tellurium (99.9%) powders at 750 °C for 72 h in an evacuated and sealed quartz ampoule. To obtain $MoTe_2$ single crystals, approximately 2 g of polycrystalline $MoTe_2$ powder and a small amount of iodine (99.8%, 4 mg/cm^3) were sealed in an evacuated quartz ampoule of 170 mm in length and 13 mm in

diameter. The ampoule was placed in a horizontal furnace with a temperature gradient so that the end containing the $MoTe_2$ charge maintained a temperature of 1000 °C, while the opposite end was kept at about 950 °C. After 168 hours in the furnace, the ampoule was quenched in ice-water and the $MoTe_2$ single crystalline platelets were extracted. According to $\theta - 2\theta$ XRD scans, the platelets crystallized in the $1T'$ form with the lattice parameters a = 6.339(3) Å, b = 3.466(4) Å, c = 13.844(3) Å, and β = 93.84(5)°.

Following structural characterization, the bulk $1T'$-$MoTe_2$ crystal was mechanically exfoliated using tape and deposited onto Si/SiO_2 substrates with an oxide thickness of 285 nm. Atomic force microscopy (AFM) images (Fig. 1a) indicated that the flake we studied is ≈ 120 nm thick (Fig. 1b) and therefore lies well within the bulk regime, implying that interactions with the substrate can be neglected. It is notable that both the starting crystal and bulk flake we studied were exposed to atmosphere for prolonged periods of time, which is known to oxidize defects in $2H$-$MoTe_2$.[40] A recent study demonstrated a similar effect in $1T'$-$MoTe_2$ where the Raman signal degraded during measurement, presumably due to photooxidation.[16] In order to avoid these effects, we performed all Raman experiments in vacuum and verified that our signal does not degrade after numerous cooldowns and measurements.

Raman measurements were performed from 5 K to 320 K on a home-built, confocal microscope integrated with a closed-cycle cryostat. The excitation source was a 532 nm laser focused through a 0.5 NA long working distance objective with a 50X magnification. Since the sample was excited in a backscattering geometry, we could detect Raman modes with A_g and B_g symmetry for $1T'$ and A_1 and B_1 symmetry modes for T_d. The laser spot diameter was ≈ 1.5 μm and the laser power was ≈1.4 mW at the sample for all measurements. Raman scattering from the sample was directed to a 500 mm focal length spectrometer with a LN_2 cooled CCD. The spectrometer and camera were calibrated using a Hg-Ar atomic line source and the spectrometer grating was positioned so that each Raman spectrum included the filtered laser line, allowing us to easily account for any drift in the laser wavelength. The instrumental response function (IRF) for these measurements was ≈ 3.9 cm^{-1}.

III. RESULTS AND DISCUSSION

We present an example Raman spectrum acquired at 5 K in Fig. 1c, at which point $MoTe_2$ is in the T_d phase. We observe four prominent peaks at ≈ 130 cm^{-1}, 165 cm^{-1}, 254 cm^{-1}, and 264 cm^{-1}, all with A_1 symmetry, which we refer to as Peaks 1–4, respectively. There is also a weak feature at 190 cm^{-1} that has B_1 symmetry, but its signal is not sufficient for temperature-dependent analysis. These assignments are based on polarization-dependent Raman measurements of the $1T'$ phase at 300 K, which will be reported elsewhere, and density functional theory calculations of the phonon eigenspectrum.[17] The Raman tensors for the $A_g(B_g)$ modes and the $A_1(B_1)$ modes are identical in structure for the backscattering configuration used here, which implies that they will evolve into an $A_1(B_1)$ symmetry at low temperature (Supporting Information).

As we increase the sample temperature from 5 K to 320 K, all peaks soften although the magnitude of the redshift is different for each. In Fig. 2a we present temperature-dependent Raman spectra for Peak 2 along with Lorentzian fits (black curves). Fig. 2b shows similar data for Peaks 3 and 4, and all spectra in Fig. 2 have been normalized by the intensity of Peak 2. A similar analysis of Peak 1 is presented in the Supporting Information.

We find that the full width at half maximum (FWHM) linewidth of Peak 1 does not change substantially over the entire temperature range (Fig. 2c). The FWHM of Peak 2 is limited by the IRF and also exhibits modest temperature dependence, which suggests that phonon-phonon interactions are weak for these modes. Peaks 3 and 4 exhibit markedly different behavior. As the sample temperature increases, these modes both redshift substantially and the FWHM linewidth of Peak 3 broadens (Fig. 2d). We quantify this behavior by fitting Peaks 3 and 4 to a double Lorentzian function plus a linear background, which allows us to extract the center frequency, amplitude, and linewidth of each mode. At 5 K, the IRF limits the FWHM of Peak 3, which is narrower than Peak 4 ($\approx 4\ \mathrm{cm}^{-1}$ versus $\approx 9\ \mathrm{cm}^{-1}$). However, Peak 3 steadily broadens with increasing temperature from 5 K to 250 K, at which point the two modes have similar linewidths. Over the same temperature range, the amplitude of Peak 4 decreases, becoming comparable to that of Peak 3 by 250 K (Fig. 2e). It is notable that observed changes in peak intensity and linewidth correlate well with the $T_d \rightarrow 1T'$ transition temperature,[15,20–23,25] suggesting that the relative intensity and linewidth of Peaks 3 and 4 are sensitive to the change in structural phase.

The frequency of all examined Raman peaks softens with increasing temperature (Fig. 3). Temperature-induced shifts in Raman frequencies are typically fit using the linear Grüneisen model:[41–44]

$$\omega(T) = \omega_o + \chi T\,. \tag{1}$$

$\omega(T)$ is the temperature-dependent phonon frequency, ω_o is the harmonic phonon frequency at 0 K, and χ is the first order temperature coefficient. The Grüneisen model combines the effects of thermal expansion and the phonon self-energy into χ and is sufficient when $T > > \frac{\hbar\omega_o}{2k_B}$ where k_B is the Boltzmann constant. At lower temperatures, $\omega(T)$ can become nonlinear and Eq. 1 is not necessarily valid. We illustrate this explicitly in Fig. 3, where the dashed line is a fit of Eq. 1 to the data from 100 K to 200 K. While there is good agreement at low $T < 100$ K for Peaks 1 and 2 (Figs. 3a and 3b), large deviations exist in this range for Peaks 3 and 4 (Figs. 3c and 3d). The fact that the linewidths of Peaks 1 and 2 exhibit comparably little variation suggests that thermal expansion and/or electron-phonon coupling, rather than phonon-phonon interactions, dominate anharmonic effects in these modes. For Peaks 3 and 4, we suggest that thermal expansion of the lattice makes a negligible contribution to the phonon frequency, and instead changes in the phonon self-energy from anharmonic coupling between different phonon branches are the dominant effect.[45] Theoretical work by Balkanski et al. demonstrated that the temperature dependence of optical phonons can be accounted for by a decay pathway resulting in multiple acoustic phonons.[39] $\omega(T)$ in this formalism is given by

$$\omega(T) = \omega_B + A\left(1 + \frac{2}{e^x - 1}\right) \quad (2)$$

Where $x = \frac{\hbar\omega_B}{2k_BT}$ and ω_B is the 0 K harmonic phonon frequency. In the treatment by Ref. 39, the constant A represents an anharmonic contribution to the frequency involving the decay of an optical phonon into two acoustic phonons. At $T = 0$, $\omega(0) = \omega_B + A$, which implies that A represents a third order correction to the phonon self-energy.[39] This model has been successfully applied to a variety of nanomaterials to explain nonlinear temperature dependence in optical phonon frequencies.[42,45–48]

We fit the frequencies of Peaks 1–4 (Figs. 3a - 3d) to Eq. 2 up to 250 K in order to isolate the T_d crystal phase. The extracted values of A, ω_B, χ, and ω_o are summarized in Table I and compared to bulk 2H-MoS_2.[45] We find that Peaks 3 and 4 have larger values of A which, when combined with the significant changes in FWHM, suggest that phonon interactions dominate the anharmonic coupling. Note that an additional term in Eq. 2 corresponding to fourth order processes has been omitted as it was not required to fit our data.[39] Furthermore, we observe that all four modes deviate from both Eqs. 1 and 2 above $T \approx 250$ K, which we interpret as the onset of the $1T'$ phase with distinct anharmonic behaviors. The unique behavior of Peaks 3 and 4 is attributed to the apparent sensitivity of their atomic displacements to interlayer coupling. As T_d transitions to $1T'$, the a and b lattice parameters increase by 0.0198 Å and 0.0375 Å, respectively, while the c lattice parameter decreases by 0.0447 Å.[38] This implies that the dominant changes are in the directions of the b lattice vector and the out-of-plane c lattice vector. Furthermore, the angle between the b and c lattice vectors changes from 90° in T_d to 93.84° in $1T'$.[38] These combined structural changes imply that phonon modes sensitive to interlayer coupling will be most affected by the $T_d \rightarrow 1T'$ transition. Peak 2 depends only weakly on the number of layers,[13] and therefore it is expected to respond minimally to changes in layer alignment and separation. In contrast, Peaks 3 and 4 are sensitive to flake thickness[13] and are therefore likely to respond to changes in the spacing and alignment of the layers during the $T_d \rightarrow 1T'$ transition.

IV. CONCLUSION

In summary, we have investigated anharmonicity of the optical phonon modes in bulk T_d-$MoTe_2$. Changes in phonon frequency, linewidth, and amplitude are determined for four modes and the results correlate well with the $T_d \rightarrow 1T'$ structural phase transition. $\omega(T)$ is nonlinear for two modes, which is consistent with an anharmonic contribution arising from optical phonon decay into multiple acoustic phonons. The large changes in frequency and linewidth for these two modes as $T_d \rightarrow 1T'$ indicates they are highly sensitive to interlayer separation and alignment, an observation that is consistent with prior characterizations of their dependence on layer number. All four modes exhibit a change in slope and an increase in frequency at $T \approx 250$ K which we attribute to the $T_d \rightarrow 1T'$ structural phase transition. These results highlight the important, and in some cases dominant, role of phonon-phonon interactions in T_d-$MoTe_2$. Further studies connecting the atomic displacement of these

modes to their anharmonicity are desirable and additional investigation of suspended, few-layer $MoTe_2$ will illuminate the impact of interlayer coupling on anharmonicity in this exciting material.

Supplementary Material

Refer to Web version on PubMed Central for supplementary material.

ACKNOWLEDGMENTS

J.J., I.S., and P.M.V. acknowledge support from the Office of Naval Research through grant N-00014-15-1-2357 and from the GMU OSCAR Program. R.B. thanks the National Research Council Research Associateship Programs for its support.

REFERENCES

1. Mak KF, Lee C, Hone J, Shan J, and Heinz TF, Physical Review Letters 105, 136805 (2010). [PubMed: 21230799]
2. Splendiani A, Sun L, Zhang Y, Li T, Kim J, Chim C-Y, Galli G, and Wang F, Nano Letters 10, 1271 (2010). [PubMed: 20229981]
3. Yang J, Lü T, Myint YW, Pei J, Macdonald D, Zheng J-C, and Lu Y, ACS Nano 9, 6603 (2015). [PubMed: 26039551]
4. Gutiérrez HR, Perea-Ló N, Elías AL, Berkdemir A, Wang B, Lv R, López-Urías F, Crespi VH, Terrones H, and Terrones M, Nano Letters 13, 3447 (2013). [PubMed: 23194096]
5. Chhowalla M, Shin HS, Eda G, Li L-J, Loh KP, and Zhang H, Nature Chemistry 5, 263 (2013).
6. Wang QH, Kalantar-Zadeh K, Kis A, Coleman JN, and Strano MS, Nature Nanotechnology 7, 699 (2012).
7. Geim AK and Grigorieva IV, Nature 499, 419 (2013). [PubMed: 23887427]
8. Mak KF and Shan J, Nature Photonics 10, 216 (2016).
9. Wilson J and Yoffe A, Advances in Physics 18, 193 (1969).
10. Dawson WG and Bullett DW, Journal of Physics C: Solid State Physics 20, 6159 (1987).
11. K.C. S, Zhang C, Hong S, Wallace RM, and Cho K, 2D Materials 2, 035019 (2015).
12. Li Y, Duerloo K-AN, Wauson K, and Reed EJ, Nature Communications 7, 10671 (2016).
13. Keum DH, Cho S, Kim JH, Choe D-H, Sung H-J, Kan M, Kang H, Hwang J-Y, Kim SW, Yang H, Chang KJ, and Lee YH, Nature Physics 11, 482 (2015).
14. Park JC, Yun SJ, Kim H, Park J-H, Chae SH, An S-J, Kim J-G, Kim SM, Kim KK, and Lee YH, ACS Nano 9, 6548 (2015). [PubMed: 26042796]
15. Qi Y, Naumov PG, Ali MN, Rajamathi CR, Schnelle W, Barkalov O, Hanfland M, Wu S-C, Shekhar C, Sun Y, Süβ V, Schmidt M, Schwarz U, Pippel E, Werner P, Hillebrand R, Förster T, Kampert E, Parkin S, Cava RJ, Felser C, Yan B, and Medvedev SA, Nature Communications 7, 11038 (2016).
16. Naylor CH, Parkin WM, Ping J, Gao Z, Zhou YR, Kim Y, Streller F, Carpick RW, Rappe AM, Drndić M, Kikkawa JM, and Johnson ATC, Nano Letters, acs.nanolett.6b01342 (2016).
17. Sun Y, Wang Y, Sun D, Carvalho BR, Read CG, Lee C.-h., Lin Z, Fujisawa K, Robinson JA, Crespi VH, Terrones M, and Schaak RE, Angewandte Chemie International Edition 55, 2830 (2016). [PubMed: 26804980]
18. Cho S, Kim S, Kim JH, Zhao J, Seok J, Keum DH, Baik J, Choe D-H, Chang KJ, Suenaga K, Kim SW, Lee YH, and Yang H, Science 349, 625 (2015). [PubMed: 26250680]
19. Duerloo K-AN, Li Y, and Reed EJ, Nature Communications 5, 4214 (2014).
20. Hughes HP and Friend RH, Journal of Physics C: Solid State Physics 11, L103 (1978).
21. Zandt T, Dwelk H, Janowitz C, and Manzke R, Journal of Alloys and Compounds 442, 216 (2007).

22. Zhang K, Bao C, Gu Q, Ren X, Zhang H, Deng K, Wu Y, Li Y, Feng J, and Zhou S, (2016), arXiv:1606.05071.
23. Chen S-Y, Goldstein T, Ramasubramaniam A, and Yan J, (2016), arXiv:1602.03566.
24. Clarke R, Marseglia E, and Hughes HP, Philosophical Magazine Part B 38, 121 (1978).
25. Wang YY, Li AZ, Wang YH, Liang Y, Jiang J, Nan HY, Ni ZH, Wang D, Zhong B, and Wen GW, Materials Research Express 3, 025007 (2016).
26. Manolikas C, van Landuyt J, and Amelinckx S, Physica Status Solidi (a) 53, 327 (1979).
27. Sun Y, Wu S-C, Ali MN, Felser C, and Yan B, Physical Review B 92, 161107 (2015).
28. Soluyanov AA, Gresch D, Wang Z, Wu Q, Troyer M, Dai X, and Bernevig BA, Nature 527, 495 (2015). [PubMed: 26607545]
29. Chang T-R, Xu S-Y, Chang G, Lee C-C, Huang S-M, Wang B, Bian G, Zheng H, Sanchez DS, Belopolski I, Alidoust N, Neupane M, Bansil A, Jeng H-T, Lin H, and Zahid Hasan M, Nature Communications 7, 10639 (2016).
30. Xu N, Wang ZJ, Weber AP, Magrez A, Bugnon P, Berger H, Matt CE, Ma JZ, Fu BB, Lv BQ, Plumb NC, Radovic M, Pomjakushina E, Conder K, Qian T, Dil JH, Mesot J, Ding H, and Shi M, (2016), arXiv:1604.02116.
31. Belopolski I, Xu S-Y, Ishida Y, Pan X, Yu P, Sanchez DS, Neupane M, Alidoust N, Chang G, Chang T-R, Wu Y, Bian G, Zheng H, Huang S-M, Lee C-C, Mou D, Huang L, Song Y, Wang B, Wang G, Yeh Y-W, Yao N, Rault JE, Fèvre PL,Bertran F, Jeng H-T, Kondo T, Kaminski A, Lin H, Liu Z, Song F, Shin S, and Hasan MZ, (2016), arXiv:1604.07079.
32. Wu Y, Jo NH, Mou D, Huang L, Bud'ko SL, Canfield PC, and Kaminski A, (2016), arXiv:1604.05176.
33. Wang C, Zhang Y, Huang J, Nie S, Liu G, Liang A, Zhang Y, Shen B, Liu J, Hu C, Ding Y, Liu D, Hu Y, He S, Zhao L, Yu L, Hu J, Wei J, Mao Z, Shi Y, Jia X,Zhang F, Zhang S, Yang F, Wang Z, Peng Q, Weng H, Dai X, Fang Z, Xu Z, Chen C, and Zhou XJ, (2016), arXiv:1604.04218.
34. Deng K, Wan G, Deng P, Zhang K, Ding S, Wang E, Yan M, Huang H, Zhang H, Xu Z, Denlinger J, Fedorov A, Yang H, Duan W, Yao H, Wu Y, Fan y. S., Zhang H, Chen X, and Zhou S, (2016), arXiv:1603.08508.
35. Liang A, Huang J, Nie S, Ding Y, Gao Q, Hu C, He S, Zhang YY, Wang C, Shen B, Liu J, Ai P, Yu L, Sun X, Zhao W, Lv S, Liu D, Li C, Zhang YY, Hu Y, Xu Y, Zhao L, Liu G, Mao Z, Jia X, Zhang F, Zhang S, Yang F, Wang Z, Peng Q, Weng H, Dai X, Fang Z, Xu Z, Chen C, and Zhou XJ, (2016), arXiv:1604.01706.
36. Jiang J, Liu ZK, Sun Y, Yang HF, Rajamathi R, Qi YP, Yang LX, Chen C, Peng H, Hwang CC, Sun SZ, Mo SK, Vobornik I, Fujii J, Parkin SSP, Felser C, Yan BH, and Chen YL, (2016), arXiv:1604.00139.
37. Huang L, McCormick TM, Ochi M, Zhao Z, Suzuki M.-t., Arita R, Wu Y, Mou D, Cao H, Yan J, Trivedi N, and Kaminski A, (2016), arXiv:1603.06482.
38. Tamai A, Wu QS, Cucchi I, Bruno FY, Ricco S, Kim TK, Hoesch M, Barreteau C, Giannini E, Bernard C, Soluyanov AA, and Baumberger F, (2016), arXiv:1604.08228.
39. Balkanski M, Wallis R, and Haro E, Physical Review B 28, 1928 (1983).
40. Chen B, Sahin H, Suslu A, Ding L, Bertoni MI, Peeters FM, and Tongay S, ACS Nano 9, 5326 (2015). [PubMed: 25868985]
41. Jana MK, Singh A, Late DJ, Rajamathi CR, Biswas K, Felser C, Waghmare UV, and Rao CNR, Journal of Physics: Condensed Matter 27, 285401 (2015). [PubMed: 26102263]
42. Łapińska A, Taube A, Judek J, and Zdrojek M, The Journal of Physical Chemistry C 120, 5265 (2016).
43. Pawbake A, Pawar M, Jadkar SR, and Late DJ, Nanoscale, 3008 (2016). [PubMed: 26782944]
44. Late DJ, Shirodkar SN, Waghmare UV, Dravid VP, and Rao CNR, ChemPhysChem 15, 1592 (2014). [PubMed: 24692405]
45. Su L, Zhang Y, Yu Y, and Cao L, Nanoscale 6, 4920 (2014). [PubMed: 24676020]
46. Taube A, L apińska A, Judek J, and Zdrojek M, Applied Physics Letters 107, 013105 (2015).
47. Duzynska A, Judek J, and Zdrojek M, Applied Physics Letters 105, 213105 (2014).

48. Taube A, Judek J, Jastrzbski C, Duzynska A, Świtkowski K, and Zdrojek M, ACS Applied Materials and Interfaces 6, 8959 (2014). [PubMed: 24897497]

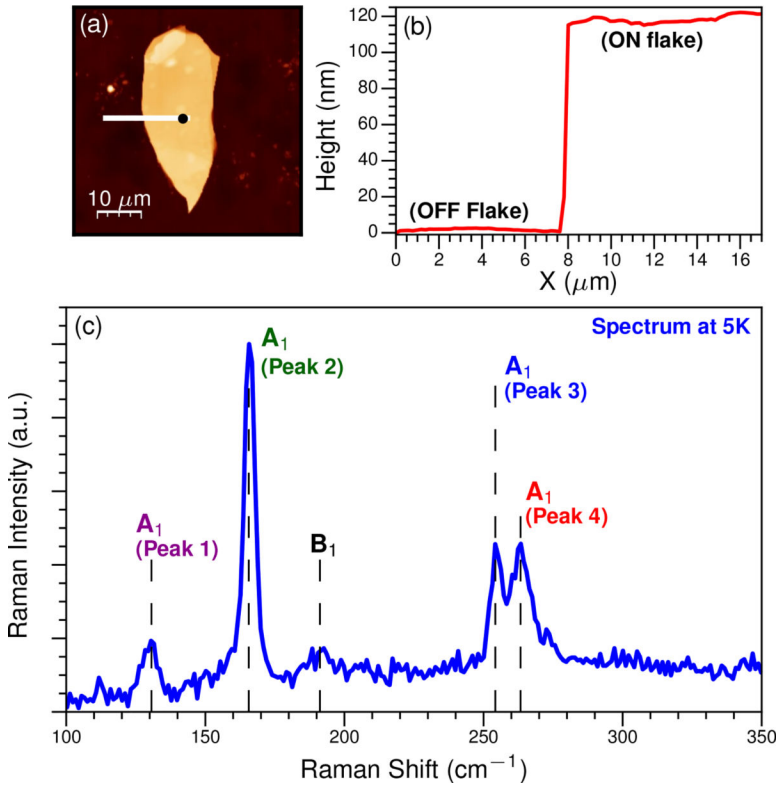

FIG. 1.

(a) AFM image of the $MoTe_2$ flake on a Si/SiO_2 substrate. The black circle on the flake marks the location where Raman spectra were acquired. (b) Height profile of the $MoTe_2$ flake extracted from (a) along the white line. The flake is over 100 nm thick, which corresponds to the bulk regime. (c) Raman spectra of T_d-$MoTe_2$ acquired at 5 K. The four peaks examined in this study are labeled along with the symmetry assignments.

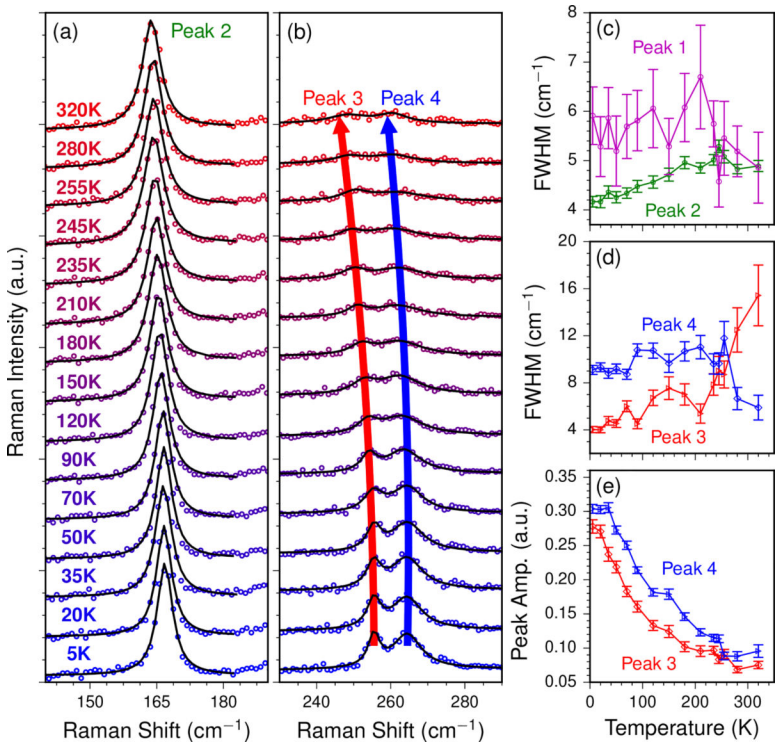

FIG. 2.

Temperature-dependent Raman spectra for (a) Peak 2 and (b) Peaks 3 and 4. Spectra are fit to either a single or double Lorentzian function with a linear background. The sample temperature increases from 5 K (bottom) to 320 K (top). In both panels, the spectra have been normalized by the intensity of Peak 2. Similar data for Peak 1 is presented in the Supporting Information. (c) FWHM of Peaks 1 and 2 extracted from the fits versus temperature. (d) FWHM of Peaks 3 and 4 extracted from the fits versus temperature. (e) Amplitudes of Peaks 3 and 4 extracted from the fits versus temperature. 1σ error bars are included in panels (c) - (e).

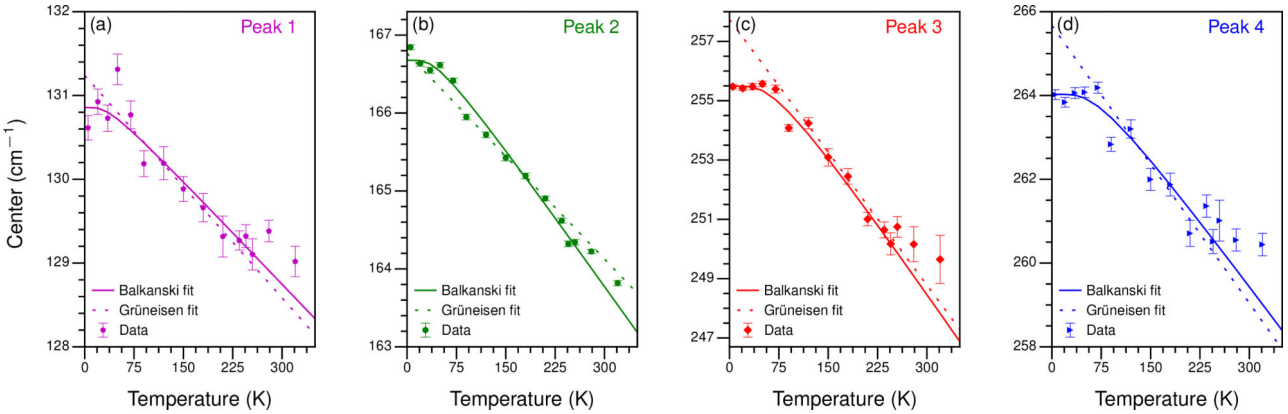

FIG. 3.

Raman frequency versus temperature for (a) Peak 1, (b) Peak 2, (c) Peak 3, and (d) Peak 4. In each panel, we fit the data to the Grüneisen model (dashed lines) in Eq. 1 from 100 – 200 K and to Eq. 2 (solid lines) from 0 – 250 K. The best fits are extrapolated over the entire temperature range and 1σ error bars are included.

TABLE I.

Measured values of A, ω_B, χ, and ω_o for Peaks 1–4 along with literature values for bulk 2H-MoS_2.

Mode	Material	Ref.	A (cm^{-1})	ω_B (cm^{-1})	χ (cm^{-1}/K)[a]	ω_o (cm^{-1})[a]
Peak 1	Bulk T_d-$MoTe_2$	this work	−0.390 ± 0.027	131.25 ± 0.091	−0.0089 ± 0.004	131.24 ± 0.537
Peak 2	”	”	−0.717 ± 0.009	167.39 ± 0.022	−0.0089 ± 0.001	166.77 ± 0.122
Peak 3	”	”	−3.019 ± 0.094	258.51 ± 0.116	−0.0312 ± 0.002	257.91 ± 0.303
Peak 4	”	”	−2.052 ± 0.105	266.08 ± 0.140	−0.0227 ± 0.003	265.74 ± 0.438
A_{1g}	Bulk 2H-MoS_2	45	−5.687	-	−0.0197	-
E^1_{2g}	”	”	−3.058	-	−0.0221	-

[a]Calculated from fits to data from 100 K to 200 K.